Nanoscale

PAPER

View Article Online
View Journal | View Issue

Cite this: *Nanoscale*, 2021, **13**, 4195

Intercalation–deintercalation of water-in-salt electrolytes in nanoscale hydrophobic confinement†

Harender S. Dhattarwal, [a] Richard C. Remsing[b] and Hemant K. Kashyap *[a]

Received 16th November 2020,
Accepted 18th January 2021

DOI: 10.1039/d0nr08163a

rsc.li/nanoscale

Intercalation–deintercalation of water-in-salt (WIS) electrolytes in nanoscale confinement is an important phenomenon relevant to energy storage and self-assembly applications. In this article, we use molecular simulations to investigate the effects of intersurface separation on the structure and free energy underlying the intercalation–deintercalation of the Li bis(trifluoromethane)sulfonimide ([Li][TFSI]) water-in-salt (WIS) electrolyte confined between nanoscale hydrophobic surfaces. We employ enhanced sampling to estimate the free energy profiles for the intercalation behaviour of WIS in confining sheets at several intersurface separations. We observe that the relative stability of the condensed and vapour phases of WIS in the confinement depends on the separation between the confining surfaces and the WIS concentration. We find that the critical separation at which the condensed and vapour phases are equally stable in confinement depends on the concentration of WIS. The relative height of the free energy barrier also strongly depends on the concentration of [Li][TFSI] inside the confined space, and we find that this concentration dependence can be attributed to changes in line tension. The process of deintercalation passes through vapour tube formation inside the confined space, and this process is initiated by vapour bubble formation. The size of the critical vapour tube required for spontaneous evaporation of WIS from the confinement is also found to depend on the intersurface separation and WIS concentration.

1 Introduction

Despite many excellent properties exhibited by water,[1] it is often discarded as a potential solvent in electrochemical energy devices because of its narrow electrochemical stability window.[1–3] Traditional liquid battery electrolytes contain salt solutions with low to moderate ion concentrations.[3] Water-in-salt (WIS) electrolytes are a new class of electrolytes which contain more salt than water by weight and volume.[4] Recent studies have shown that superconcentrated water-in-salt electrolytes exhibit enhanced redox stability, low volatility, high carrier density, a wide electrochemical window and efficient cycling behaviour.[1,4–8] Recently, WIS solutions have been extensively studied in bulk as well in confinement.[2,9–13]

The intercalation–deintercalation behaviour of the ions of liquid electrolytes plays an important role in tailoring the properties of electrochemical devices.[14–16] It has been found that in a Li-ion battery containing highly concentrated electrolytes, reversible accommodation of Li^+ ions in graphite can significantly change the electrode behaviour and can lead to fast electrode reactions.[6] The interaction of the solution confined between ionophobic nanoscale materials results in a capillary force driving the deintercalation of the electrolyte from nanoporous electrodes,[17] self-assembly of nanomaterials,[18–20] and many other physical phenomena.[16,21–26] Exfoliation of layered compounds can also be tuned by intercalation of the solution between hydrophobic surfaces.[27–29] However, before studying the intercalation behaviour in the presence of electric field it is important to first understand the process at zero applied field. Past theoretical studies show that the intercalation of water and salt solutions in solvophobic confinements is enhanced when local electric field is applied.[30,31]

The vapour phase of solvents in nanoscale solvophobic confinement becomes more stable when the confining surfaces come in close proximity, below a critical separation.[32–36] Strong electric fields stabilize the vapour phase in nanoscale confinement.[31] Many recent theoretical studies show that the transition between the vapour phase and liquid phase of water confined between parallel plates is separated by a barrier, where the condensed phase is more stable at higher plate sep-

[a]*Department of Chemistry, Indian Institute of Technology Delhi, Hauz Khas, New Delhi 110016, India. E-mail: hkashyap@chemistry.iitd.ac.in; Fax: +91-(0)11-26581102; Tel: +91-(0)11-26591518*

[b]*Department of Chemistry and Chemical Biology, Rutgers University, Piscataway, NJ 08854, USA*

†Electronic supplementary information (ESI) available. See DOI: 10.1039/D0NR08163A

arations and the vapour phase is more stable at lower plate separations.[35,37–39] It is found that the capillary evaporation of water originates from the formation of isolated vapour cavities on the plates, which grow to a gap-spanning vapour tube that eventually fills the entire volume between the confining sheets.[37] Altabet *et al.* showed through forward flux sampling that the formation of vapour bubbles and vapour tubes are important milestones in the process of capillary evaporation of water from hydrophobic sheets.[39] They also showed that the rate of capillary evaporation of water from hydrophobic flexible confinement is increased by multiple folds with increased flexibility of confining sheets. However, analogous theoretical studies exploring the process of capillary evaporation in superconcentrated aqueous solutions are scarce in the literature. Herein, we have performed detailed enhanced molecular dynamics simulations to examine the dewetting behaviour of [Li][TFSI] WIS solution from nanoscale hydrophobic confinement. We study the effect of interplate separation as well as WIS concentration on the free energy underlying the intercalation–deintercalation transition of WIS from confinement. We also compare our results with available macroscopic theories wherever possible.

Our results suggest that capillary evaporation of the WIS from hydrophobic confinement proceeds similar to what is observed for water confined between hydrophobic surfaces.[37,39] However, because of the complex structural changes, the changes in the underlying free energy are not well-described by a single macroscopic thermodynamic free energy surface at larger separations. The relative stability of WIS in the confinement significantly depends on WIS concentration. It is observed that at a given interplate separation, lowering the WIS concentration enhances its propensity to leave the confinement. It is also revealed that the change in the barrier of the free energy is dictated by the *line tension* and not by the contact angle and surface tension that are often thought to be governing factors for better material design.

2 Simulation details

In the present investigation, we have performed classical atomistic molecular dynamics (MD) simulations combined with non-Boltzmann sampling techniques to investigate the deintercalation of WIS from rigid nanoscale carbon surfaces. A pair of carbon surfaces (having dimension of 3 nm × 3 nm) separated by a distance d nm in the y-direction were generated using an in-house program and placed in the WIS solution along the xz-plane in a 6.5 nm × 13 nm × 6.5 nm tetragonal box. Each surface consists of three hexagonally packed parallel sheets (lattice constant 0.142 nm). In order to maintain a pressure equal to that of liquid–vapour coexistence, a similar protocol was followed as reported in previous studies.[35,37,38] A snapshot depicting the simulation setup for two carbon surfaces separated by a distance, d = 1.3 nm inside the WIS electrolyte, is shown in Fig. S1.† For the highest separations studied here, d = 1.7 nm, different systems having varying concentration of aqueous salt (here [Li][TFSI]) solutions were prepared. The details of the concentration of the WIS solutions for all the systems investigated in the present study are provided in Table S1.†

All MD simulations were performed using the GROMACS 2019.[40,41] The systems were first equilibrated for 5 ns in the NVT ensemble at 310 K temperature. The temperature of all the systems was maintained using a Nosé–Hoover[42,43] thermostat. Following equilibration, biased simulations were carried out for 10 ns. The equations of motion were integrated using the leap-frog algorithm with a time step of 1 fs. The last 5 ns of each trajectory, saved every 100 fs, was used for the analysis. The cutoff radius for the evaluation of short-ranged interactions was set to 1.2 nm. Coulomb interactions were evaluated using the particle mesh Ewald summation technique with an interpolation order of 6 and a Fourier grid spacing of 0.08 nm.

The force field parameters for Li^+ and $[TFSI]^-$ were taken from OPLS-AA force-fields.[44–46] The TIP3P model was employed for the water molecules.[47] The non-bonded interaction parameters for the carbon sheet atoms were taken as σ = 0.355 nm (ref. 48) and ε = 0.022 kJ mol^{-1}.[38] The Lorentz–Berthelot combination rules were used to compute cross interaction terms of LJ potentials. Standard 3D periodic boundary conditions and minimum image convention were applied.

The indirect umbrella sampling (INDUS) approach was used to sample the density fluctuations between the confining surfaces, using a harmonic biasing potential, $U(\tilde{N}) = \kappa(\tilde{N} - \tilde{N}^*)^2/2$. Here, $\tilde{N}$ is a coarse-grained, continuous variant of the order parameter N, which is the number of species confined between the two surfaces for varying intersurface separation, d.[49,50] The INDUS potential was applied only on the Li^+ ion, the nitrogen atom of $[TFSI]^-$, and the oxygen atom of water molecules. N^* is the target value of order parameter for each biased simulation and we vary it over a range of −3 to 213 with an interval of 3. The free energy, ΔG, underlying deintercalation of the WIS was estimated from the INDUS simulations using the weighted histogram analysis method (WHAM).[51] Five hundred thousand frames for each trajectory were used to compute the free energy profiles.

3 Results and discussion

3.1 Thermodynamics of WIS intercalation

In order to understand the WIS intercalation in nanoscale hydrophobic carbon sheets, we sampled the system at different numbers of confined species between the surfaces, N, for five different confinement separations, d. The free energy, ΔG, is plotted as a function of N for all d-values in Fig. 1. Here, in the region of both high and low N values, we observe minima in free energy profiles. The minima in the region of high N values correspond to the condensed phase of the WIS in confinement. The local density of the WIS inside the confinement at these points is comparable to the WIS density outside the confinement (see Fig. S2†). Note that all the pro-

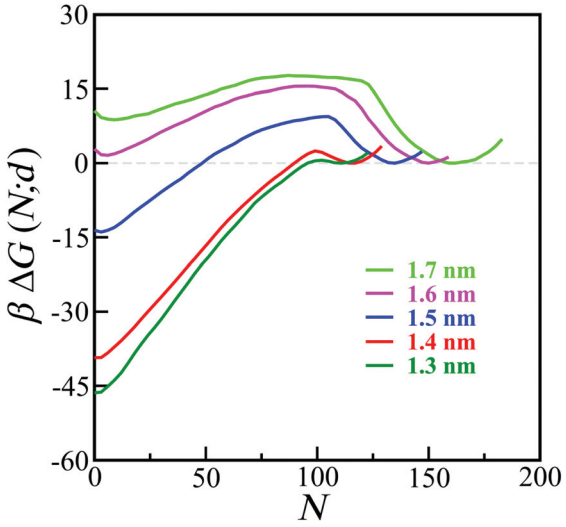

Fig. 1 The simulated free energy profiles as a function of number of molecules in the confinement at different separations, d, for 20 m WIS.

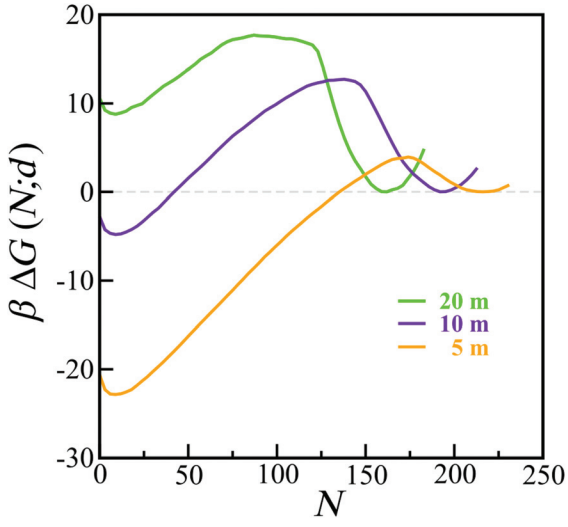

Fig. 2 The simulated free energy profiles as a function of number of molecules in the confinement for different concentrations of the WIS for separation d = 1.7 nm.

files are shifted to set the free energy of the condensed basin equal to zero. As N lowers, the confined solution moves towards the vapour phase. The minima in the region of low N values correspond to the vapour phase of the WIS in confinement. These condensed (high N) and vapour (low N) basins are separated by a substantial free energy barrier. The height of the barrier increases with an increase in the separation between the confining surfaces. Note that the change from condensed to vapour phase represents the process of deintercalation of the WIS from the confinement, whereas the change from vapour to condensed phase depicts the intercalation of the WIS, including Li^+ ions, into the confinement.

At lower separations, *e.g.* d = 1.3 nm, the vapour phase of the WIS is stable in confinement. Also, the free energy barrier to the transition from condensed to vapour phase is minuscule, and spontaneous deintercalation can occur. The relative free energy of the vapour phase increases with increasing d. The critical distance, d_c, is defined as the separation between the confining sheets at which both the condensed and vapour phases have the same free energy, which is located at a value of d slightly less than 1.6 nm. Above d_c, the condensed phase becomes more stable with respect to the vapour phase. At larger separations, the vapour phase is *meta*-stable in the confinement.

The solution concentration can also affect the intercalation–deintercalation free energy of the WIS in confinement. We quantify this concentration dependence of $\Delta G(N)$ at d = 1.7 nm, which is shown in Fig. 2 for the WIS concentrations of 20 m, 10 m, and 5 m. For the concentration of 10 m, the relative free energy of the vapour phase of WIS is less than that of the condensed phase. This suggests that for this concentration the critical separation, d_c, is now more than 1.7 nm. At even lower concentration, 5 m, the free energy barrier between the condensed and vapour phases decreases further. We anticipate that at sufficiently lower concentration the deintercalation process of the WIS from carbon surfaces separated by a distance, d = 1.7 nm, may be spontaneous. We note that similar results have been found for denaturants in water, where an increase in guanidinium chloride concentration is found to weaken hydrophobic effects.[52,53]

The intersurface separation has a significant impact on the free energy barrier separating the condensed and vapour phases in confinement. For example, at fixed concentration (20 m), the free energy barrier separating the condensed and vapour phases increases with increasing d. To further quantify the effect of intersurface separation on the height of the free energy barrier, we plot the barrier height, ΔG^*, as a function of d in Fig. 3. The height of the free energy barrier is predicted by macroscopic theory to scale quadratically with d, according to:[35,37]

$$\beta\Delta G^*(d) = -\frac{2\pi\beta\gamma_{vl}}{\cos\theta}\left[\frac{\tilde{d}^2}{4} + \tilde{d}\left(\frac{\lambda}{\gamma_{vl}}\right) + \left(\frac{\lambda}{\gamma_{vl}}\right)^2\right], \quad (1)$$

where $\beta^{-1} = k_BT$ is Boltzmann's constant multiplied by temperature, γ_{vl} is the vapour liquid surface tension, θ is the contact angle, λ is the line tension, and $\tilde{d} = d - \xi$ is the distance available between the sheets, which accounts for the effective size of the sheet atoms. We approximate this size as the sum of the van der Waals radii of a sheet atom and the smallest WIS particle, Li^+, such that $\xi = \sigma_C + \sigma_{Li}$; σ_C and σ_{Li} are the LJ size parameters for the sheet carbon atom and the Li^+ ion, respectively. We estimated the contact angles (θ) formed by the WIS nanodroplets at the carbon surface and the vapour–liquid interfacial surface tension (γ_{vl}) for different WIS concentrations from independent simulations, and these are reported in the ESI.† The line tension was treated as a fit parameter, and we obtain a negative line tension, $\lambda/\gamma_{vl} \approx -0.325$ nm, which is

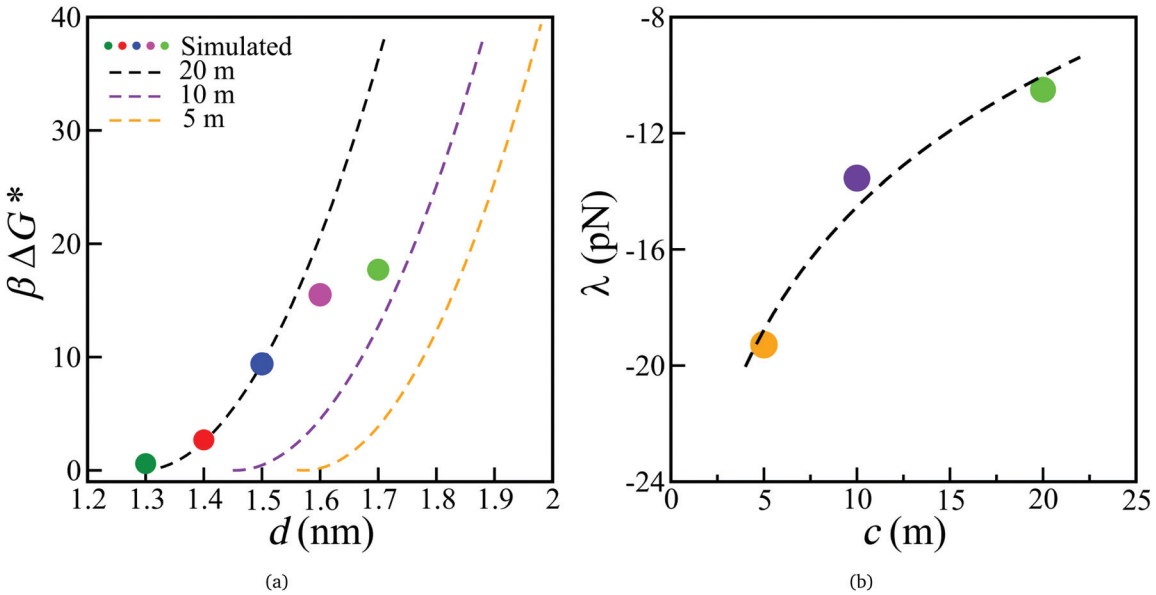

Fig. 3 (a) The free energy barrier of transition from condensed to vapour phase as a function of confining sheet separation, d, as well as the predictions of eqn (1). Predictions for 5 m and 10 m WIS solutions are obtained by matching the simulated barrier at d = 1.7 nm. (b) The line tension, λ, obtained from macroscopic theory at d = 1.7 nm is plotted for different concentrations, assuming that the simulated free energy agrees with the macroscopic theory for 5 m and 10 m WIS solutions.

roughly half of that for water in a similar environment, as estimated in previous work.[37]

Water and simple liquids follow this classical macroscopic expectation for most values of d.[37] However, confinement-induced changes in the microscopic water structure can lead to deviations from macroscopic theory at small d.[54] Substantial deviations from macroscopic theory have also been observed for ionic liquids, which were also attributed to d-dependent structural changes of the confined liquid.[35] Here, we find that the free energy barriers follow eqn (1) to a good approximation for smaller d-values, where the solution structure is similar (discussed below). However, the barrier height deviates from the classical predictions at higher separations. These deviations can be attributed to changes in the relative concentration and distribution of the species in confinement at different separations, consistent with previous work.[35,54]

We also include the predictions of eqn (1) for the 10 m and 5 m systems in Fig. 3, obtained by fitting the line tension to the simulation results, assuming that d = 1.7 nm agrees with the theory for these two concentrations. Decreasing the WIS concentration lowers the barrier height, as discussed above, and the use of eqn (1) enables a macroscopic interpretation of this dependence. Upon decreasing the WIS concentration, both the surface tension and $1/\cos\theta$ increase in magnitude, further increasing $\Delta G^*(d)$, in stark contrast to what we observe. However, the line tension increases in magnitude from $\lambda/\gamma_{vl} \approx -0.325$ nm to $\lambda/\gamma_{vl} \approx -0.405$ nm to $\lambda/\gamma_{vl} \approx -0.549$ nm upon decreasing the concentration from 20 m to 10 m to 5 m, respectively. Thus, the line tension becomes increasingly negative as concentration is decreased, approaching that of pure water ($\lambda/\gamma_{vl} \approx -0.65$ nm to -0.75 nm),[37] as shown in Fig. 3(b). Assuming that adsorption at the three-phase contact line follows a Langmuir isotherm, the concentration-dependence can be described well by the Szyszkowski equation:[55–57]

$$\lambda(c) = \lambda_0 - k_B T \Gamma_\infty \ln(1 + Kc), \quad (2)$$

where c is the concentration, λ_0 is the line tension for pure water as obtained previously,[37] and $\Gamma_\infty \approx -16.3$ nm^{-1} and $K \approx 1.00093$ m^{-1} (inverse molal) are fit parameters; the fit is shown in Fig. 3(b). This concentration-dependence of the line tension compensates for and overcomes the changes in surface tension and contact angle that tend to increase the barrier height, resulting in lower free energy barriers at lower concentrations. Therefore, from the perspective of macroscopic interfacial thermodynamics, the lowering of free energy barriers with decreasing WIS concentration can be attributed, at least in part, to the concentration-dependence of the line tension.

3.2 Structure of WIS inside confinement

Recent studies show that structural changes influence the kinetics of capillary evaporation of water and ionic liquids from the nanoscale hydrophobic confinement.[35,39] Moreover, the local density distribution plays an important role in governing the relative stability of species between the hydrophobic carbon surfaces. Number density profiles of constituent species of WIS between the carbon surfaces are depicted in Fig. 4(a). The number density distributions are evaluated for systems with N corresponding to the condensed phase of WIS in confinement.

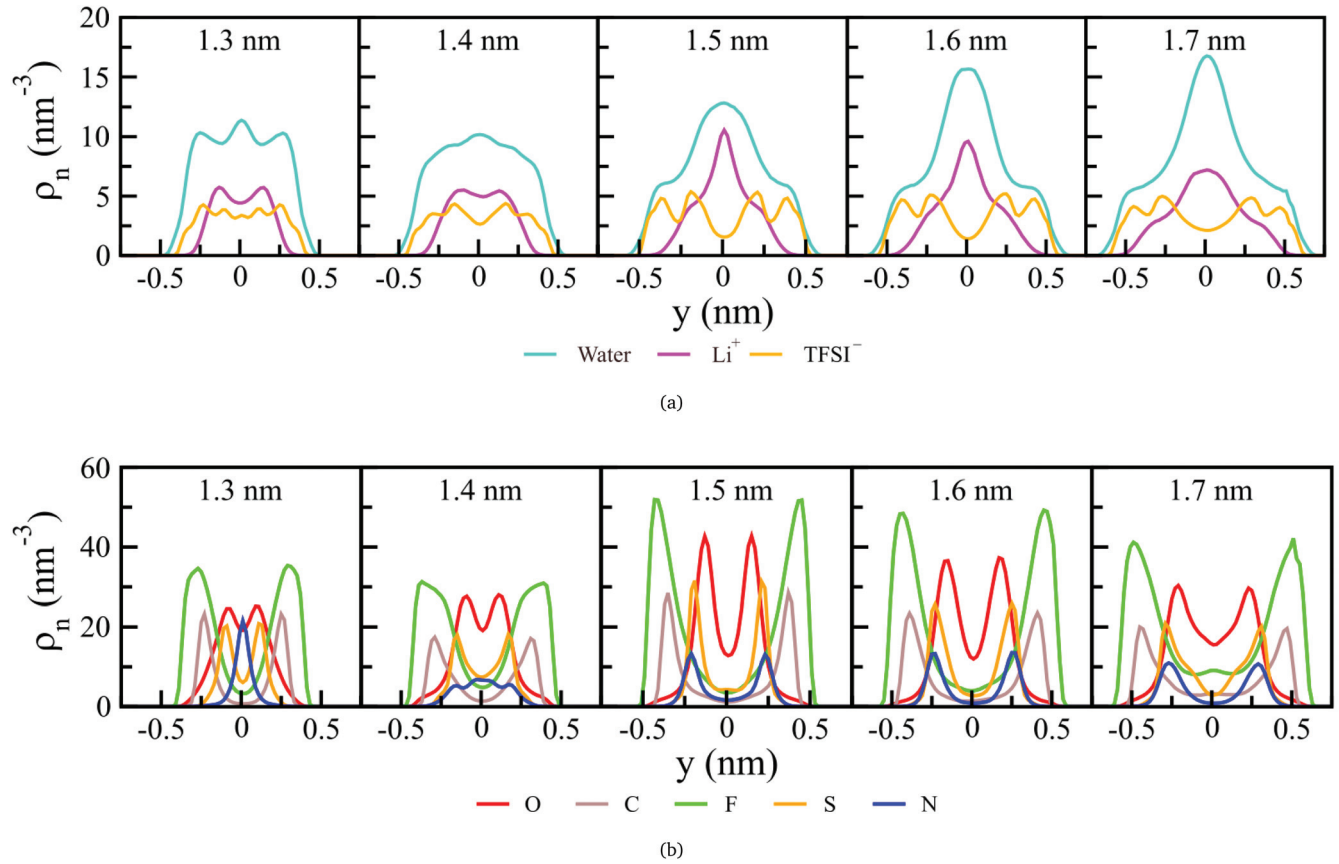

Fig. 4 Number density distribution of (a) water, Li^+, and $[TFSI]^-$ and (b) atomic species of $[TFSI]^-$ for 20 m WIS, computed for configurations with *N* corresponding to the condensed phase between hydrophobic nanoscale confinement.

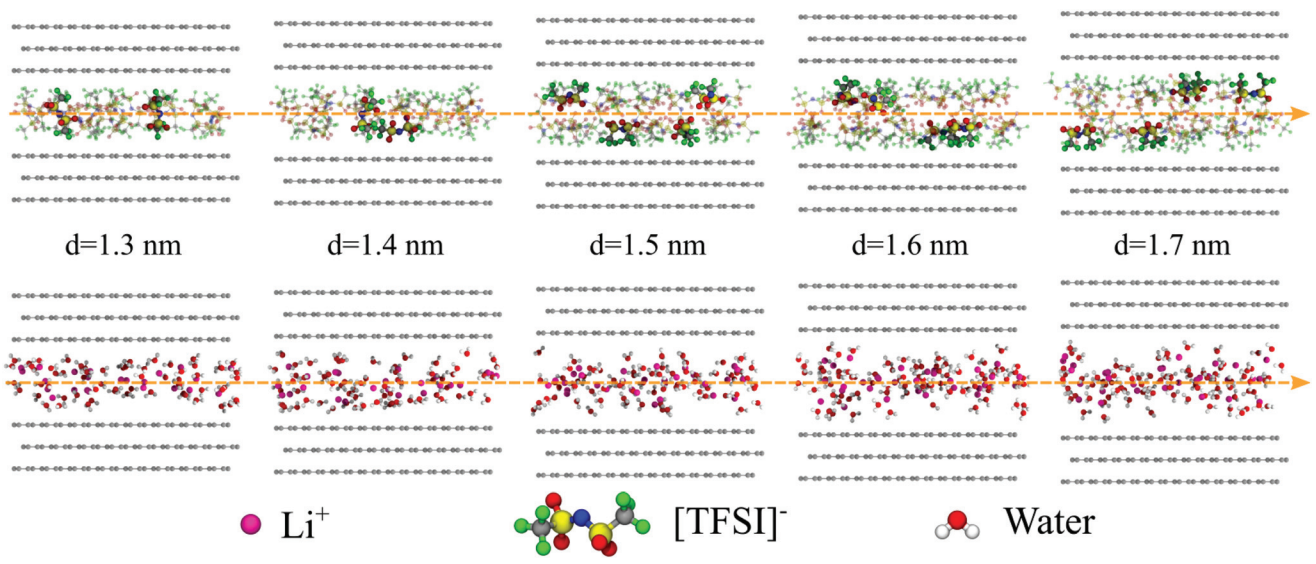

Fig. 5 Simulation snapshots of WIS species inside the hydrophobic sheets separated by a distance *d* corresponding to 20 m concentration of WIS. Blue, red, yellow, grey, and green colours represent the N, O, S, C, and F atoms, respectively.

For d = 1.3 nm, the density profiles show that the Li^+ cations preferentially reside away from the confining surface. However, the water molecules are distributed throughout the confined space, as is the case for the anions. The simulation snapshots in Fig. 5 show that the anions are oriented perpendicular to the confining sheets at this interplate spacing. The

nitrogen atoms lie around the center of the confinement, and the fluorine atoms are nearest to the opposite surfaces. The orientation of the anions is also confirmed by plotting atomic number density profiles for $[TFSI]^-$ anions, shown in Fig. 4(b). Here, a peak for the number density distribution at $y = 0$ affirms that the nitrogen atoms align at the confinement center.

The structural arrangement of $[TFSI]^-$ ions for $d = 1.4$ nm is almost similar to $d = 1.3$ nm, but the increased space allows some of the anions to tilt (shown in Fig. 5). This tilting smears out the density distributions, especially for the nitrogen atom. This starts to signal that the structure is changing from a single layer of plate-bridging anions to two layers. There are three peaks for nitrogen atoms that are merged, where the central peak corresponds to the perpendicular orientation of $[TFSI]^-$, and the two side peaks to the tilted orientations.

At higher separation, $d = 1.5$ nm, the number density profiles show that the Li^+ ions and water molecules are shifted towards the center of the confinement. The $[TFSI]^-$ ions show two peaks close to both carbon surfaces. The atomic number density profile of $[TFSI]^-$ ions depicted in 4(b) shows sharp peaks for all atoms, indicating highly ordered distributions of anions in confinement. Two peaks for nitrogen atoms show that the anions form a bilayer distribution. The CF_3 groups are closest to the carbon surfaces and the SO_2 groups are oriented towards the center of the confinement. The space between the two layers of $[TFSI]^-$ ions is occupied by the Li^+ ions and water molecules. The simulation snapshots for $d = 1.5$ nm (see Fig. 5) illustrate the presence of empty space around the central line passing through the $[TFSI]^-$ ions. The Li^+ ions and water molecules reside around this central line.

The species exhibit similar distributions at higher separations, $d = 1.6$ nm and 1.7 nm. However, the space between the two layers of $[TFSI]^-$ ions increases with increasing interplate separation. This results in an increased number of water molecules inside the confinement (see Table 1). We suggest that these structural changes underlie the deviations of the free energy barriers from macroscopic theory discussed in the previous section.

The fraction of [Li][TFSI] ion pairs relative to water molecules as a function of N, $x_{IP:Wat}(N)$, quantifies any preference for one component of the solution to intercalate over the other. As shown in Fig. S7 of the ESI,† $x_{IP:Wat}(N)$ shows a preferential deintercalation of ion pairs once a vapour tube is formed, evidenced by $x_{IP:Wat}(N)$ decreasing with decreasing N.

Table 1 The number of [Li][TFSI] ion pairs and water molecules in the condensed phase of WIS inside the confinement at different interplate separations

d (nm)	N_{IP}	N_{Wat}	$x_{IP:Wat}$
1.3	22	67	0.33
1.4	24	68	0.35
1.5	30	73	0.41
1.6	33	83	0.40
1.7	34	92	0.37

For small d (1.4 nm), $x_{IP:Wat}$ decreases slightly as N decreases (deintercalation) for all N, indicating that [Li][TFSI] has a higher tendency to come out of the confinement when the energy barrier is smaller. At larger d values (1.5–1.7 nm), $x_{IP:Wat}$ initially increases as N is lowered from the value in the condensed phase. Then, $x_{IP:Wat}$ starts decreasing once the barrier separating condensed and vapour phases is crossed.

3.3 Shapes of free energy profiles

In order to further understand the shape of the free energy profiles, we examined the nature of the vapour regions that form in the confined space, following previous work.[37] We provided instantaneous liquid–vapour interface representations[58] (see Fig. 6) to illustrate how the shape of the vapour-like region changes as the WIS deintercalates from the hydrophobic confinement of interplate separation $d = 1.5$ nm. For $N = 135$, corresponding to the condensed phase, the WIS fills the space between the confining plates. However, for $N = 117$, uphill from the condensed phase, vapour bubbles start to appear on the carbon surfaces. The solvophobic carbon sheets enhance nearby WIS density fluctuations, and these enhanced fluctuations facilitate the preferential nucleation of surface vapour bubbles. These bubbles then grow to form a vapour tube that spans across the confinement. At $N = 105$, near the energy barrier, the size of the gap-spanning vapour tube is subcritical. The vapour tube has to grow further to become supercritical. Once the gap-spanning vapour tube becomes supercritical, the dewetting of WIS from the surface is spontaneous. However, for $d = 1.5$ nm, the size difference between subcritical and supercritical vapour tubes is small. Furthermore, the vapour tube grows between the confinement ($N = 54$) and eventually covers the volume between two surfaces ($N = 3$).

Our findings can be compared to macroscopic interfacial thermodynamics, where the free energy for the formation of a cylindrical vapour tube with radius r, which spans between two surfaces separated by a distance d, is given by:[37]

$$\Delta G_{th}(r;d) = \pi[r^2\tilde{d}\Delta P + 2r\tilde{d}\gamma_{vl} + 2r^2\gamma_{vl}\cos\theta + 4r\lambda], \quad (3)$$

where ΔP is the difference between the system pressure and the saturation pressure, here equal to zero. Classical interfacial thermodynamics shows that the condensed/liquid phase ($r = 0$) and the vapour phase (high r values) are separated by a barrier that corresponds to vapour tube formation.

Significant changes appear in the free energy profiles as the number of species in confinement is decreased. The slope of the profiles has an abrupt discontinuity at or in the vicinity of the barrier. In the free energy profiles for water evaporation from rigid hydrophobic carbon plates, there exists a "kink" corresponding to the transition of surface bubbles to gap-spanning vapour tubes. It manifests the intersection of distinct free energy profiles for surface bubble formation and vapour tube expansion.[37] Altabet *et al.* show in their study of water evaporation from flexible hydrophobic confinement using the forward flux sampling technique that this transition from the liquid to vapour phase passes through the milestone of gap-

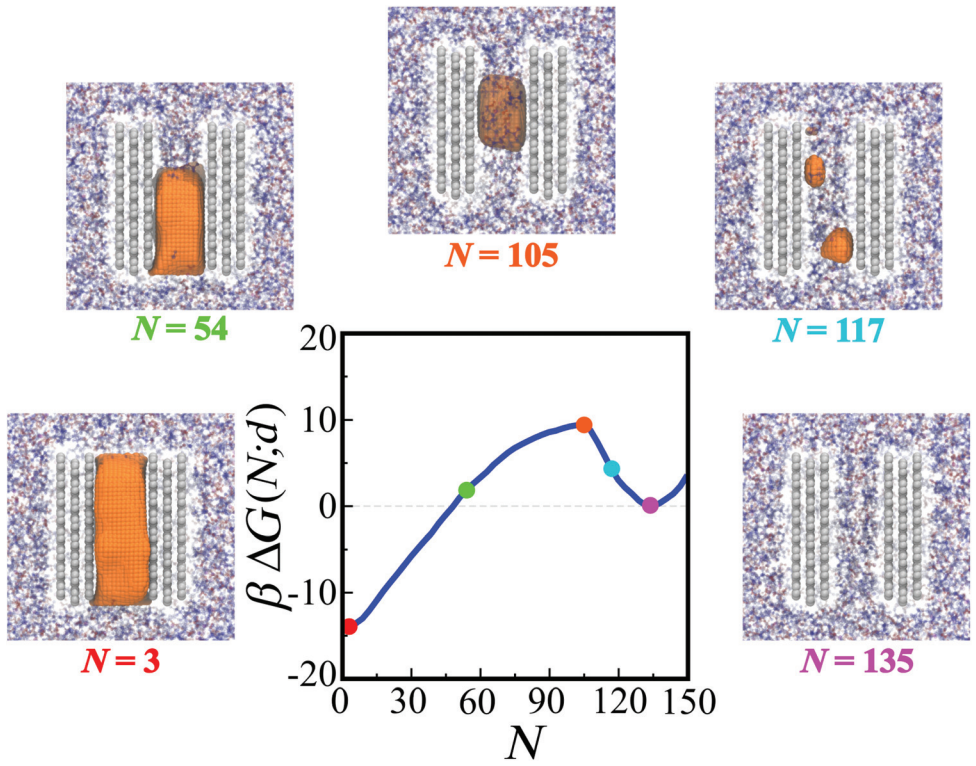

Fig. 6 The instantaneous liquid–vapour interface at different points along the free energy profile for d = 1.5 nm.

spanning vapour bridge formation between the opposite sheets.[39]

For the 20 m WIS electrolyte, we find that eqn (3), with an additional entropic term[37] as discussed in the ESI,† provides a reasonable fit to the vapour tube growth portion of the free energies, for N less than the kink, when $d \leq 1.5$ nm, as shown in Fig. 7. For larger d-values, significant structural changes can occur as N is decreased, modifying interfacial thermodynamic properties. We find that $\Delta G(N)$ for large d is better fit by two vapour tube free energies that intersect at $N \approx N_{\text{super}}$, unlike what is observed for water over a large range of d values.[37] This piecewise fit is given by $\Delta G_{\text{p}}(r;d) = \Delta G_{\text{th}}^{(1)}(r;d) - 2k_{\text{B}}T\ln(1-2r/L)$ for $N < N_{\text{super}}$ and $\Delta G_{\text{p}}(r;d) = \Delta G_{\text{th}}^{(2)}(r;d) - 2k_{\text{B}}T\ln(1-2r/L)$ for $N_{\text{super}} < N < N_{\text{sub}}$, where L = 3 nm is the side length of the square confining plates,

$$\Delta G_{\text{th}}^{(\text{i})}(r;d) = 2\pi\gamma_{\text{vl}}^{(i)}\left[r^2\cos\theta + r\left(\tilde{d} + \frac{2\lambda^{(i)}}{\gamma_{\text{vl}}^{(i)}}\right)\right], \quad (4)$$

$\gamma_{\text{vl}}^{(\text{i})}$ and $\lambda^{(\text{i})}$ indicate that the fits yield different values of the surface and line tensions in the two ranges of N, and the logarithmic terms capture the translational entropy of the tube. The fit parameters are listed in Table S3 of the ESI.†

The free energy profiles show that the process of deintercalation of WIS from nanoscale hydrophobic confinement has two major processes at small d, but three at large d. Firstly, the transition from vapour bubble formation at the hydrophobic surfaces to gap-spanning vapour tube is a steep uphill process. Subsequently, the vapour tube grows, resulting in capillary evaporation of WIS from the confinement. The vapour tube formed may have to first grow for the process of capillary evaporation to become spontaneous. Whether the vapour tube formed at the kink in the free energy is supercritical depends on the interplate separation as well as the WIS concentration. The vapour tube formed between the surfaces separated by 1.4 nm (Fig. 7(a)) is sufficient for further dewetting of WIS from the surfaces; the deintercalation process is spontaneous. For d = 1.6 nm (Fig. 7(b)), the vapour tube formed is subcritical and must grow in size before spontaneous capillary evaporation occurs. Moreover, for the highest separation and concentration studied here, d = 1.7 nm (20 m), the gap between the subcritical and supercritical vapour tube sizes increases further (see Fig. 7(c)). For this system, and d = 1.6 nm, the gap region and the supercritical growth region are described well by two intersecting vapour tube macroscopic free energies, ΔG_{p}, and we suggest that the transition between the two surfaces arises from structural changes in the confined solution as N decreased, consistent with previous observations for ionic liquids.[35,38] However, if the concentration of the WIS is lowered to 5 m, the vapour tube formed at the kink is supercritical (see Fig. 7(d)).

In the case of hydrophilic surfaces, the vapour state becomes unstable even at lower d values; thus the deintercalation of WIS from the hydrophilic confinement is not spontaneous. For a hydrophobic surface, $\cos\theta < 0$, while for a hydrophilic surface, $\cos\theta > 0$. In eqn (3) with $\Delta P = 0$, $\cos\theta < 0$

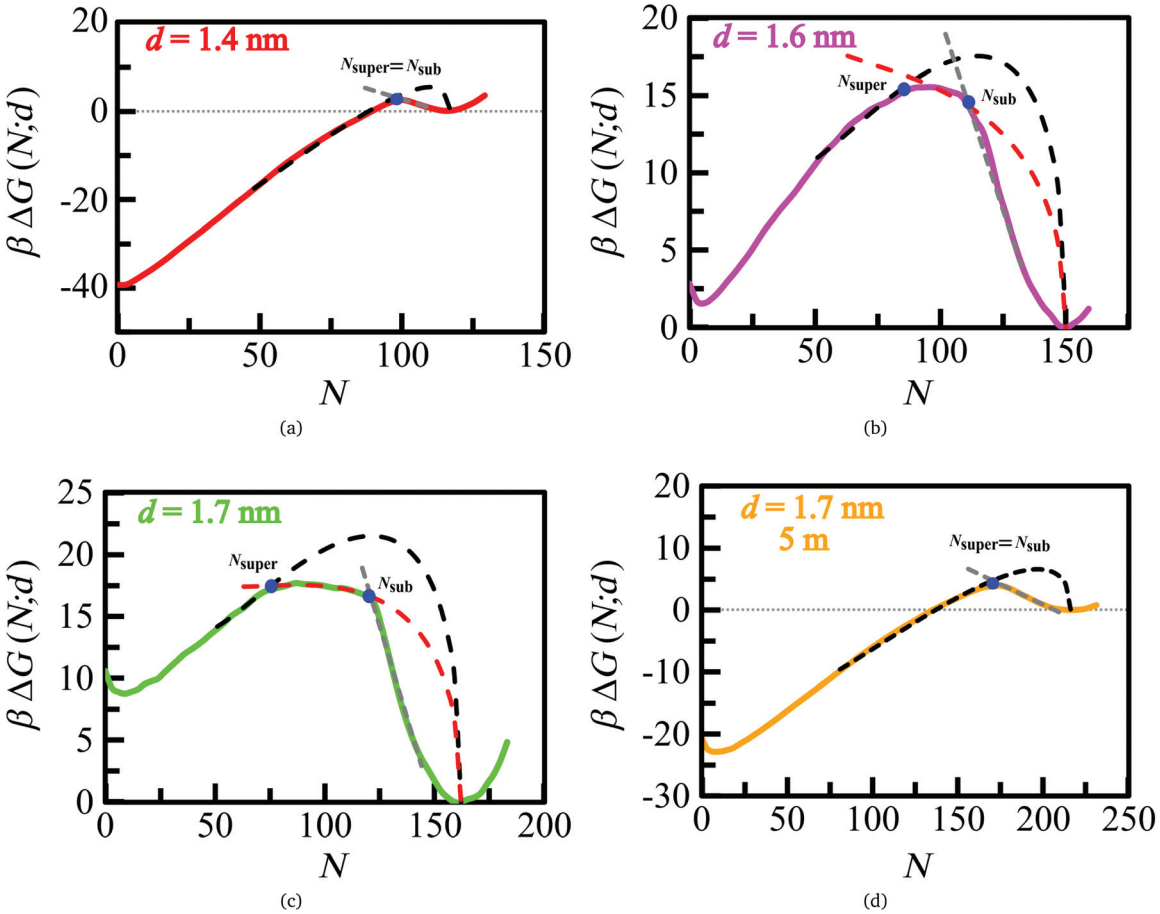

Fig. 7 The simulated free energy profile for (a) d = 1.4 nm (solid red line), (b) d = 1.6 nm (solid pink line), (c) d = 1.7 nm and 20 m WIS concentration (solid green line), and (d) d = 1.7 nm and 5m WIS concentration (solid orange line). The free energy for vapour bubble formation (grey dashed line) which is linear at lower N values of liquid basin ($\Delta G(N;d) = aN + b$), growth of subcritical (red dashed line) and supercritical vapour tube (black dashed line) predicted from macroscopic theory. The fit parameters are listed in Table S3 of the ESI.†

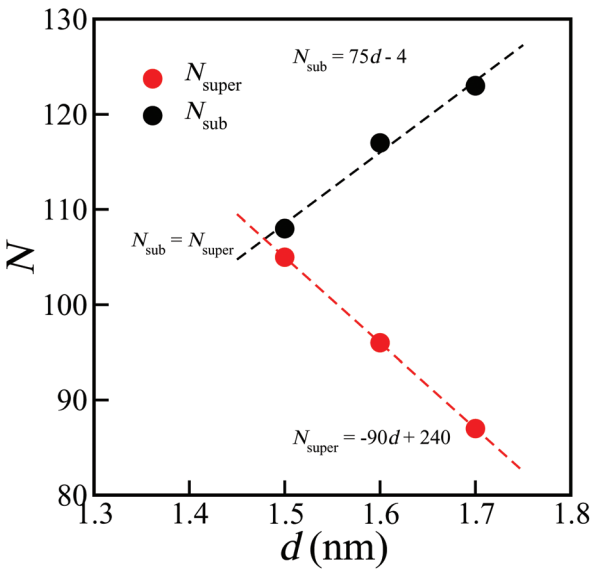

Fig. 8 The number of molecules inside the confinement at the points when the size of the gap-spanning vapour tube is of subcritical and supercritical size for different interplate separations.

yields a $\Delta G_{th}(r)$ consistent with a barrier like those shown in Fig. 7. In contrast, a hydrophilic surface with $\cos\theta > 0$ flips the parabola such that there is no barrier and no competition with the linear surface tension term; the condensed phase, r = 0, is favoured and the vapour is unstable.

The number of species present inside the confinement at the point of subcritical and supercritical vapour tube formation is plotted for different interplate separations in Fig. 8, for separations where $N_{sub} \neq N_{super}$. We observe that the point of subcritical vapour tube formation increases linearly with d

Table 2 The number of species confined between hydrophobic sheets, and free energy values when the vapour tube is subcritical and supercritical

d (nm)	N_{CP}	N_{sub}	$\beta\Delta G_{sub}$	N_{super}	$\beta\Delta G_{super}$
1.4	117	99	2.5	99	2.5
1.5	135	108	8.78	105	9.4
1.6	150	117	12.61	96	15.53
1.7	165	123	15.86	87	17.68

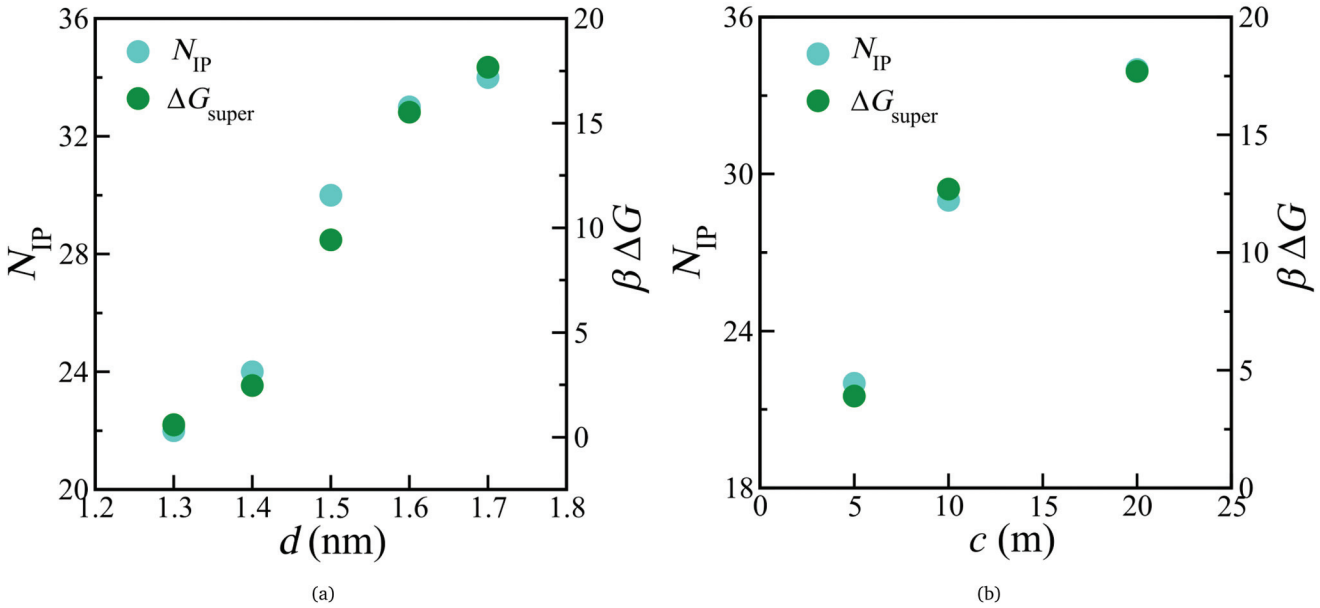

Fig. 9 The simulated free energy corresponding to the N value for the formation of a gap-spanning vapour tube, and the corresponding number of [Li][TFSI] ion pairs in confinement plotted for (a) different interplate separations for 20 m WIS solution, and (b) different concentration of the WIS between sheets separated by 1.7 nm. The ΔG_{super} is plotted against the N_{IP} of the condensed phase in Fig. S8 of the ESI.†

for nanoscale confinements, whereas the point of supercritical tube formation decreases linearly with d, *i.e.*, the gap-spanning vapour tube needs to grow bigger as the interplate separation increases before spontaneous evaporation can occur. If we extrapolate both fittings, the intersection point (slightly less than 1.5 nm) represents the separation below which the process of capillary evaporation is spontaneous when the gap-spanning vapour tube forms inside the confinement.

The values of N for the condensed phase (CP), the subcritical and supercritical vapour tubes, and the corresponding free energies are provided in Table 2. We have plotted the simulated free energy for the N value corresponding to the formation of confinement spanning supercritical vapour tube and the number of [Li][TFSI] ion pairs between the confinement in the condensed phase between corresponding confinement for different interplate separations (for c = 20 m), and for different concentrations (d = 1.7 nm) in Fig. 9. These plots reveal that the free energy required for the formation of the supercritical vapour tube depends on the amount of salt inside the confinement in the condensed phase at a given interplate separation and WIS concentration.

4 Conclusions

The intercalation extent of [Li][TFSI] WIS in nanoscale hydrophobic confinement depends on the separation of the confining surfaces. At larger interplate separations, d = 1.7 nm, the condensed phase is more stable than vapour phase in confinement, and intercalation is favoured. At lower separations, d = 1.3–1.4 nm, the vapour phase of the WIS is more stable and deintercalation of WIS is favoured. Our results also show that the concentration of the WIS also affects the relative stability of the WIS between the sheets. We find that lowering the WIS concentration at fixed interplate separation reduces the stability of the condensed phase, enhancing the propensity for deintercalation or evaporation. Moreover, decreasing the WIS concentration lowers the free energy barrier for deintercalation. This barrier lowering is dictated by the *line tension*, not the contact angle and surface tension that are usually at the focus of material design; these tend to increase the barriers in the WIS system and are opposed by the line tension. These findings strongly suggest that both confinement length scale and solution concentration can be used to controllably tune the intercalation–deintercalation behaviour of WIS-based electrochemical devices.

We also showed that the confined WIS is highly structured. At a separation of d = 1.3 nm, the $[TFSI]^-$ anions align themselves perpendicular to the confining sheets. As the interplate separation is increased (d = 1.5 nm) the $[TFSI]^-$ anions preferentially align parallel to the sheets and the Li^+ cations, and water molecules occupy the space between the parallel $[TFSI]^-$ layers. With a further increase in interplate separation, the space between the $[TFSI]^-$ layers increases and the relative amount of water inside the confinement also increases.

Through examination of liquid–vapour instantaneous interfaces, we suggest that capillary evaporation in the WIS proceeds in a manner similar to that observed for water confined between hydrophobic surfaces,[37,39] except that structural changes as N is lowered may lead to significant changes in the form of $\Delta G(N)$ that are not well-described by a single macroscopic thermodynamic free energy surface at larger d. We

found that vapour bubbles begin to appear on the carbon surfaces as N is decreased from the condensed phase. These bubbles then grow and merge to form a gap-spanning vapour tube, resulting in a kink in the free energy profile. At lower d, the vapour tube formed at the kink is of supercritical size and results in spontaneous evaporation of the WIS in the confined space. At higher d, the size of the vapour tube is subcritical and must grow further before spontaneous evaporation can occur. The difference in the subcritical and supercritical vapour tube sizes increases with increasing interplate separation. Also, the free energy barrier for supercritical vapour tube formation is correlated with the amount of salt in confinement. Our analysis shows that the intercalation of the electrolyte in hydrophobic electrode pores can be controlled by tuning the salt concentration in the electrolyte.

Conflicts of interest

There are no conflicts to declare.

Acknowledgements

H. S. D. thanks UGC India for fellowship. The authors thank the IIT Delhi HPC facility for computational resources. This work was financially supported by Science and Engineering Research Board (SERB), Department of Science and Technology, India through the Core Research Grant (CRG/2019/000898) awarded to H. K. K.

References

1 R.-S. Kühnel, D. Reber and C. Battaglia, *J. Electrochem. Soc.*, 2020, **167**, 070544.
2 Z. Li, R. Bouchal, T. Mendez-Morales, A.-L. Rollet, C. Rizzi, S. Le Vot, F. Favier, B. Rotenberg, O. Borodin, O. Fontaine and M. Salanne, *J. Phys. Chem. B*, 2019, **123**, 10514–10521.
3 M. Chen, G. Feng and R. Qiao, *Curr. Opin. Colloid Interface Sci.*, 2020, **47**, 99–110.
4 L. Suo, O. Borodin, T. Gao, M. Olguin, J. Ho, X. Fan, C. Luo, C. Wang and K. Xu, *Science*, 2015, **350**, 938.
5 L. Suo, O. Borodin, W. Sun, X. Fan, C. Yang, F. Wang, T. Gao, Z. Ma, M. Schroeder, A. von Cresce, S. M. Russell, M. Armand, A. Angell, K. Xu and C. Wang, *Angew. Chem., Int. Ed.*, 2016, **55**, 7136–7141.
6 Y. Yamada and A. Yamada, *J. Electrochem. Soc.*, 2015, **162**, A2406–A2423.
7 Y. Yamada, K. Usui, K. Sodeyama, S. Ko, Y. Tateyama and A. Yamada, *Nat. Energy*, 2016, **1**, 16129.
8 C. Yang, J. Chen, T. Qing, X. Fan, W. Sun, A. von Cresce, M. S. Ding, O. Borodin, J. Vatamanu, M. A. Schroeder, N. Eidson, C. Wang and K. Xu, *Joule*, 2017, **1**, 122–132.
9 J. Vatamanu and O. Borodin, *J. Phys. Chem. Lett.*, 2017, **8**, 4362–4367.
10 L. Suo, D. Oh, Y. Lin, Z. Zhuo, O. Borodin, T. Gao, F. Wang, A. Kushima, Z. Wang, H.-C. Kim, Y. Qi, W. Yang, F. Pan, J. Li, K. Xu and C. Wang, *J. Am. Chem. Soc.*, 2017, **139**, 18670–18680.
11 L. Coustan, G. Shul and D. Bélanger, *Electrochem. Commun.*, 2017, **77**, 89–92.
12 N. Dubouis, P. Lemaire, B. Mirvaux, E. Salager, M. Deschamps and A. Grimaud, *Energy Environ. Sci.*, 2018, **11**, 3491–3499.
13 Z. Yu, L. A. Curtiss, R. E. Winans, Y. Zhang, T. Li and L. Cheng, *J. Phys. Chem. Lett.*, 2020, **11**, 1276–1281.
14 S. Maruyama, T. Fukutsuka, K. Miyazaki, Y. Abe, N. Yoshizawa and T. Abe, *J. Mater. Chem. A*, 2018, **6**, 1128–1137.
15 K. Ji, J. Han, A. Hirata, T. Fujita, Y. Shen, S. Ning, P. Liu, H. Kashani, Y. Tian, Y. Ito, J.-I. Fujita and Y. Oyama, *Nat. Commun.*, 2019, **10**, 275.
16 W. Lv and R. Wu, *Nanoscale*, 2013, **5**, 2765–2775.
17 K. Liu, P. Zhang and J. Wu, *J. Chem. Phys.*, 2018, **149**, 234708.
18 M. Kanduč, A. Schlaich, E. Schneck and R. R. Netz, *Langmuir*, 2016, **32**, 8767–8782.
19 J. Yin, Y. Huang, S. Hameed, R. Zhou, L. Xie and Y. Ying, *Nanoscale*, 2020, **12**, 17571–17589.
20 W. Foster, K. Miyazawa, T. Fukuma, H. Kusumaatmaja and K. Voïtchovsky, *Nanoscale*, 2020, **12**, 5452–5463.
21 D. Klinger, M. J. Robb, J. M. Spruell, N. A. Lynd, C. J. Hawker and L. A. Connal, *Polym. Chem.*, 2013, **4**, 5038–5042.
22 K. Lum, D. Chandler and J. D. Weeks, *J. Phys. Chem. B*, 1999, **103**, 4570–4577.
23 R. Xie, C. R. López-Barrón and N. J. Wagner, in *Self-Assembly of Block Copolymers in Ionic Liquids*, American Chemical Society, 2017, vol. 1250, pp. 83–142.
24 Y. Li, M. A. Alibakhshi, Y. Zhao and C. Duan, *Nano Lett.*, 2017, **17**, 4813–4819.
25 Y. Li, H. Chen, S. Xiao, M. A. Alibakhshi, C.-W. Lo, M.-C. Lu and C. Duan, *ACS Nano*, 2019, **13**, 3363–3372.
26 H. T. Kieu, B. Liu, H. Zhang, K. Zhou and A. W.-K. Law, *Appl. Surf. Sci.*, 2018, **452**, 372–380.
27 J. Wang, K. K. Manga, Q. Bao and K. P. Loh, *J. Am. Chem. Soc.*, 2011, **133**, 8888–8891.
28 Y. L. Zhong and T. M. Swager, *J. Am. Chem. Soc.*, 2012, **134**, 17896–17899.
29 A. M. Abdelkader and I. A. Kinloch, *ACS Sustainable Chem. Eng.*, 2016, **4**, 4465–4472.
30 D. Vanzo, D. Bratko and A. Luzar, *J. Phys. Chem. B*, 2015, **119**, 8890–8899.
31 D. Bratko, C. D. Daub, K. Leung and A. Luzar, *J. Am. Chem. Soc.*, 2007, **129**, 2504–2510.
32 A. Wallqvist and B. J. Berne, *J. Phys. Chem.*, 1995, **99**, 2893–2899.
33 C. A. Cerdeiriña, P. G. Debenedetti, P. J. Rossky and N. Giovambattista, *J. Phys. Chem. Lett.*, 2011, **2**, 1000–1003.
34 D. Chandler, *Nature*, 2005, **437**, 640–647.

35 G. Shrivastav, R. C. Remsing and H. K. Kashyap, *J. Chem. Phys.*, 2018, **148**, 193810.
36 X. Huang, C. J. Margulis and B. J. Berne, *Proc. Natl. Acad. Sci. U. S. A.*, 2003, **100**, 11953.
37 R. C. Remsing, E. Xi, S. Vembanur, S. Sharma, P. G. Debenedetti, S. Garde and A. J. Patel, *Proc. Natl. Acad. Sci. U. S. A.*, 2015, **112**, 8181–8186.
38 H. S. Dhattarwal, R. C. Remsing and H. K. Kashyap, *J. Phys. Chem. C*, 2020, **124**, 4899–4906.
39 Y. E. Altabet, A. Haji-Akbari and P. G. Debenedetti, *Proc. Natl. Acad. Sci. U. S. A.*, 2017, **114**, E2548–E2555.
40 H. J. C. Berendsen, D. van der Spoel and R. van Drunen, *Comput. Phys. Commun.*, 1995, **91**, 43–56.
41 D. van der Spoel, E. Lindahl, B. Hess, G. Groenhof, A. E. Mark and H. J. C. Berendsen, *J. Comput. Chem.*, 2005, **26**, 1701–1718.
42 S. Nosé, *J. Chem. Phys.*, 1984, **81**, 511–519.
43 W. G. Hoover, *Phys. Rev. A*, 1985, **31**, 1695–1697.
44 K. P. Jensen and W. L. Jorgensen, *J. Chem. Theory Comput.*, 2006, **2**, 1499–1509.
45 B. Doherty, X. Zhong, S. Gathiaka, B. Li and O. Acevedo, *J. Chem. Theory Comput.*, 2017, **13**, 6131–6145.
46 J. N. Canongia Lopes, J. Deschamps and A. A. H. Pádua, *J. Phys. Chem. B*, 2004, **108**, 2038–2047.
47 W. L. Jorgensen, J. Chandrasekhar, J. D. Madura, R. W. Impey and M. L. Klein, *J. Chem. Phys.*, 1983, **79**, 926–935.
48 S. Sharma and H. K. Kashyap, *J. Phys. Chem. C*, 2015, **119**, 23955–23967.
49 A. J. Patel, P. Varilly, D. Chandler and S. Garde, *J. Stat. Phys.*, 2011, **145**, 265–275.
50 A. J. Patel, P. Varilly and D. Chandler, *J. Phys. Chem. B*, 2010, **114**, 1632–1637.
51 S. Kumar, J. M. Rosenberg, D. Bouzida, R. H. Swendsen and P. A. Kollman, *J. Comput. Chem.*, 1992, **13**, 1011–1021.
52 J. L. England, V. S. Pande and G. Haran, *J. Am. Chem. Soc.*, 2008, **130**, 11854–11855.
53 R. Godawat, S. N. Jamadagni and S. Garde, *J. Phys. Chem. B*, 2010, **114**, 2246–2254.
54 Y. E. Altabet and P. G. Debenedetti, *J. Chem. Phys.*, 2017, **147**, 241102.
55 B. v. Szyszkowski, *Z. Phys. Chem.*, 1908, **64**, 385–414.
56 M. Haustein, M. Wahab, H.-J. Mögel and P. Schiller, *Langmuir*, 2015, **31**, 4078–4086.
57 N. D. Petsev, L. G. Leal and M. S. Shell, *Phys. Rev. Lett.*, 2020, **125**, 146101.
58 A. P. Willard and D. Chandler, *J. Phys. Chem. B*, 2010, **114**, 1954–1958.